

# We are IntechOpen, the world's leading publisher of Open Access books Built by scientists, for scientists

5,800

Open access books available

142,000

International authors and editors

180M

Downloads

Our authors are among the

154

Countries delivered to

TOP 1%

most cited scientists

12.2%

Contributors from top 500 universities



WEB OF SCIENCE™

Selection of our books indexed in the Book Citation Index  
in Web of Science™ Core Collection (BKCI)

Interested in publishing with us?  
Contact [book.department@intechopen.com](mailto:book.department@intechopen.com)

Numbers displayed above are based on latest data collected.  
For more information visit [www.intechopen.com](http://www.intechopen.com)



# One Dimensional Morphing Structures for Advanced Aircraft

Robert D. Vocke III<sup>1</sup>, Curt S. Kothera<sup>2</sup>, Benjamin K.S. Woods<sup>1</sup>,  
Edward A. Bubert<sup>1</sup> and Norman M. Wereley<sup>1</sup>

<sup>1</sup>University of Maryland, College Park, MD

<sup>2</sup>Techno-Sciences, Inc., Beltsville, MD,  
USA

## 1. Introduction

Since the Wright Brothers' first flight, the idea of "morphing" an airplane's characteristics through continuous, rather than discrete, movable aerodynamic surfaces has held the promise of more efficient flight control. While the Wrights used a technique known as wing warping, or twisting the wings to control the roll of the aircraft (Wright and Wright, 1906), any number of possible morphological changes could be undertaken to modify an aircraft's flight path or overall performance. Some notable examples include the Parker Variable Camber Wing used for increased forward speed (Parker, 1920), the impact of a variable dihedral wing on aircraft stability (Munk, 1924), the high speed dash/low speed cruise abilities associated with wings of varying sweep (Buseman, 1935), and the multiple benefits of cruise/dash performance and efficient roll control gained through telescopic wingspan changes (Sarh, 1991; Gevers, 1997; Samuel and Pines, 2007).

While the aforementioned concepts focused on large-scale, manned aircraft, morphing technology is certainly not limited to vehicles of this size. In fact, the development of a new generation of unmanned aerial vehicles (UAVs), combined with advances in actuator and materials technology, has spawned renewed interest in radical morphing configurations capable of matching multiple mission profiles through shape change - this class has come to be referred to as "morphing aircraft" (Barbarino *et al.*, 2011). Gomez and Garcia (2011) presented a comprehensive review of morphing UAVs. Contemporary research is primarily dedicated to various conformal changes, namely, twist, camber, span, and sweep. It has been shown that morphing adjustments in the planform of a wing without hinged surfaces lead to improved roll performance, which can expand the flight envelope of an aircraft (Gern *et al.*, 2002), and more specifically, morphing to increase the span of a wing results in a reduction in induced drag, allowing for increased range or endurance (Bae *et al.*, 2005). The work presented here is intended for just such a one dimensional (1-D) span-morphing application, for example a UAV with span-morphing wingtips depicted in Figure 1. By achieving large deformations in the span dimension over a small section of wing, the wingspan can be altered during flight to optimize aspect ratio for different roles. Furthermore, differential span change between wingtips can generate a roll moment, replacing the use of ailerons on the aircraft (Hetrick *et al.*, 2007). This one dimensional

morphing could also be used in the chordwise direction, and is not limited in application to fixed-wing aircraft, as rotorcraft would also benefit from a variable diameter or chord rotor.

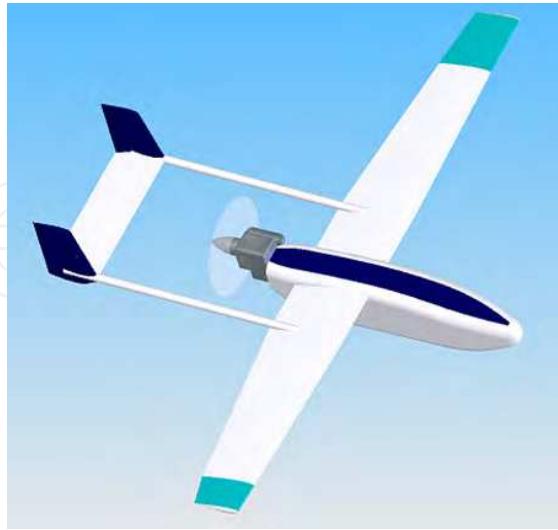


Fig. 1. Illustration of span-morphing UAV showing 1-D morphing wingtips.

A key challenge in developing a one dimensional morphing structure is the development of a useful morphing skin, defined here as a continuous layer of material that would stretch over the morphing structure and mechanism to form a smooth aerodynamic skin surface. For a span-morphing wingtip in particular, the necessity of a high degree of surface area change, large strain capability in the span direction, and little to no strain in the chordwise direction all impose difficult requirements on any proposed morphing skin. The goal of this effort was a 100% increase in both the span and area of a morphing wingtip, or “morphing cell.”

Reviews of contemporary morphing skin technology (Thill *et al.*, 2008; Wereley and Gandhi, 2010) yield three major areas of research being pursued: compliant structures, shape memory polymers, and anisotropic elastomeric skins. Compliant structures, such as the FlexSys Inc. Mission Adaptive Compliant Wing (MACW), rely on a highly tailored internal structure and a conventional skin material to allow small amounts of trailing edge camber change (Perkins *et al.*, 2004). Due to the large geometrical changes required for a span-morphing wingtip as envisioned here, metal or resin-matrix-composite skin materials are unsuitable because they are simply unable to achieve the desired goal of 100% increases in morphing cell span and area.

Shape memory polymer (SMP) skin materials are relatively new and have recently received attention for morphing aircraft concepts. They may at first glance seem highly suited to a span-morphing wingtip: shape memory polymers made by Cornerstone Research Group exhibit an order of magnitude change in modulus and up to 200% strain capability when heated past a transition temperature, yet return to their original modulus upon cooling. There have been attempts to capitalize on the capabilities of SMP skins, such as Lockheed Martin’s Z-wing morphing UAV concept (Bye and McClure, 2007) and a reconfigurable segmented variable stiffness skin composed of rigid disks and shape memory polymer proposed by McKnight *et al.* (2010). However, electrical heating of the SMP skin to reach transition temperature proved difficult to implement in the wind tunnel test article and the

SMP skin was abandoned as a high-risk option. Additionally, the state-of-the-art of SMP technology does not appear to be well-suited for dynamic control morphing objectives.

With maximum strains above 100%, low stiffness, and a lower degree of risk due to their passive operation, elastomeric materials are ideal candidates for a morphing skin. Isotropic elastomer morphing skins have been successfully implemented on the MFX-1 UAV (Flanagan *et al.*, 2007). This UAV employed a mechanized sliding spar wing structure capable of altering the sweep, wing area, and aspect ratio during flight. Sheets of silicone elastomer connect rigid leading and trailing edge spars, forming the upper and lower surfaces of the wing. The elastomer skin is reinforced against out-of-plane loads by ribbons stretched taut immediately underneath the skin, which proved effective for wind tunnel testing and flight testing. Morphing sandwich structures capable of high global strains have also been investigated (Joo *et al.*, 2009; Bubert *et al.*, 2010; Olympio *et al.*, 2010). However, suitable improvements over these structures, such as anisotropic fiber reinforcement and a better developed substructure for out-of-plane reinforcement, are desired for a fully functional morphing skin.

The present research therefore focuses on the development of a passive anisotropic elastomer composite skin with potential for use in a 1-D span-morphing UAV wingtip. The skin should be capable of sustaining 100% active strain with negligible major axis Poisson's ratio effects, giving a 100% change in surface area, and should also be able to withstand typical aerodynamic loads, assumed to range up to 200 psf (9.58 kPa) for a maneuvering flight surface, with minimal out-of-plane deflection. The following will describe the process of designing, building, and testing a morphing skin with these goals in mind, and will compare the performance of the final article to the initial design objectives.

## 2. Conceptual development

The primary challenge in developing a morphing skin suitable as an aerodynamic surface is balancing the competing goals of low in-plane actuation requirements and high out-of-plane stiffness. In order to make the skin viable, actuation requirements must be low enough that a reasonable actuation system within the aircraft can stretch the skin to the desired shape and hold it for the required morphing duration. At the same time, the skin must withstand typical aerodynamic loads without deforming excessively (e.g., rippling or bowing), which would result in degradation to the aerodynamic characteristics of the airfoil surface.

To achieve these design goals, a soft, thin silicone elastomer sheet with highly anisotropic carbon fiber reinforcement, called an elastomeric matrix composite (EMC), would be oriented such that the fiber-dominated direction runs chordwise at the wingtip, and the matrix-dominated direction runs spanwise (Figure 2a). Reinforcing carbon fibers controlling the major axis Poisson's ratio of the sheet would limit the EMC to 1-D spanwise shape change (Figure 2b). For a given skin stiffness, actuation requirements will increase in proportion to the skin thickness,  $t_s$ , while out-of-plane stiffness will be proportional to  $t_s^3$  by the second moment of the area. To alleviate these competing factors, a flexible substructure is desired (Figure 2c) that would be capable of handling out-of-plane loads without greatly adding to the in-plane stiffness. This allows a thinner skin which, in turn, reduces actuation requirements. The combined EMC sheet and substructure form a continuous span-morphing skin.

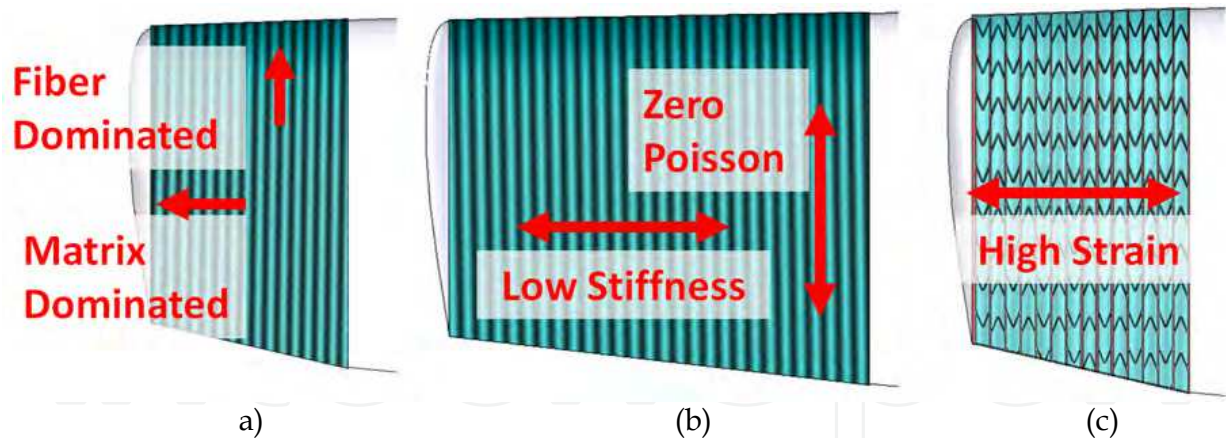


Fig. 2. Design concept as a span morphing wingtip. (Bubert *et al.*, 2010)

To motivate the goal of low in-plane stiffness for this research, the skin prototype was designed to be actuated by a span-morphing pneumatic artificial muscle (PAM) scissor mechanism described separately by Wereley and Kothera (2007). The PAM scissor mechanism shown in Figure 3 was designed to transform contraction of the PAM actuator into extensile force necessary in a span-morphing wing. Based upon the maximum performance of the PAM and the kinematics of the scissor frame, the maximum force output of the actuation system was predicted and a skin stiffness goal was determined such that 100% active strain could be achieved, with the skin simplified as having linear stiffness. A margin of 15% was added to the 100% strain goal to account for anticipated losses due to friction or manufacturing shortcomings in the skin or actuation system.

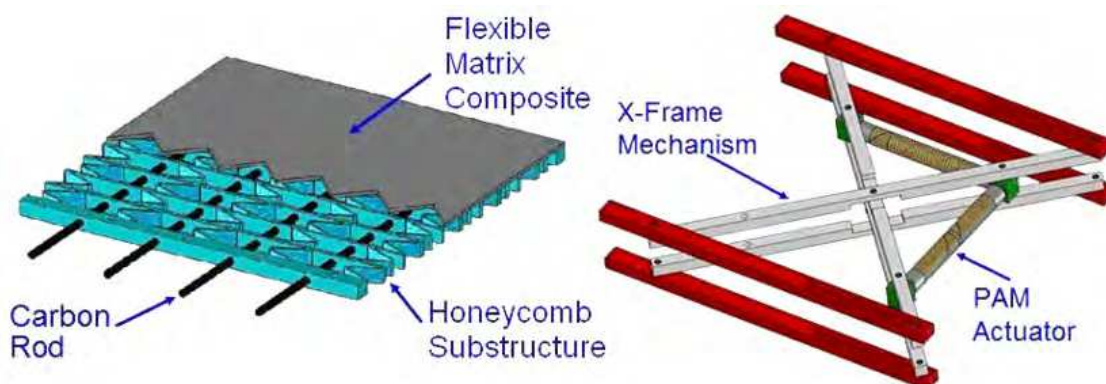


Fig. 3. Morphing skin demonstrator including PAM actuation system.

In addition, minimal out-of-plane deflection of the skin surface under aerodynamic loading was desired. No specific out-of-plane deflection goal was set or designed for, but out-of-plane stiffness of the substructure was kept in mind during the design process. Deflection due to distributed loads was included as a final test to ensure that the aerodynamic shape of a UAV wing morphing structure could be maintained during flight.

### 3. Skin development

The primary phase of the morphing skin development was to fabricate the EMC sheet that would make up the skin or face sheet. A number of design variables were available for

tailoring the EMC to the application, including elastomer stiffness, durometer, ease of handling during manufacturing, and the quantity, thickness, and angle of carbon fiber reinforcement.

### 3.1 Elastomer selection

Initially, a large number of silicone elastomers were tested for viability as matrix material. Desired properties included maximum elongation well over 100%, a low stiffness to minimize actuation forces, moderate durometer to avoid having too soft a skin surface, and good working properties. Workability became a primary challenge to overcome, as two-part elastomers with high viscosities or very short work times would not fully wet out the carbon fiber layers. While over a dozen candidate elastomer samples were examined, only four were selected for further testing. Table 1 details the silicone elastomers tested as matrix candidates.

| Material     | Modulus (kPa) | Viscosity (cP) | % Elongation at Break | Comments              |
|--------------|---------------|----------------|-----------------------|-----------------------|
| DC 3-4207    | 130           | 430            | 100+                  | difficult to demold   |
| Sylgard-186  | 410           | 65,000         | 100+                  | too viscous           |
| V-330, CA-45 | 570           | 10,000         | 500                   | excellent workability |
| V-330, CA-35 | 330           | 10,000         | 510                   | excellent workability |

Table 1. Elastomer properties.

The most promising compositions tested were Dow Corning 3-4207 series and the Rhodorsil V-330 series. Both exhibited the desired low stiffness and greater than 100% elongation, but DC 3-4207 suffered from poor working qualities and lower maximum elongation and was not down-selected. Rhodorsil's V-330 series two-part room temperature vulcanization (RTV) silicone elastomer had the desired combination of low viscosity, long working time, and easy demolding to enable effective EMC manufacture, and also demonstrated very high maximum elongation and tear strength. V-330 with CA-35 had the lowest stiffness of the two V-330 elastomers tested. This led to selecting V-330, CA-35 for use in test article fabrication.

### 3.2 CLPT predictions and validation

Concurrently, using classical laminated plate theory (CLPT), a simple model of the EMC laminate was developed to study the effects of changing composite configuration on performance. The skin lay-up shown in Figure 4a was examined: two silicone elastomer face sheets sandwiching two symmetric unidirectional carbon fiber/elastomer composite laminae. The unidirectional fiber layers are offset by an angle  $\theta_i$  from the 1-axis, which corresponds to the chordwise direction. Orienting the fiber-dominated direction along the wing chord controls minor Poisson's ratio effects while retaining low stiffness and high strain capability in the 2-axis, which corresponds to the spanwise direction.

In order to determine directional properties of the EMC laminate, directional properties of each lamina must first be found. The following micromechanics derivation comes from Agarwal *et al.* (2006). For a unidirectional sheet with the material longitudinal (L) and transverse (T) axes oriented along the fiber direction as shown in Figure 4b, we assume that

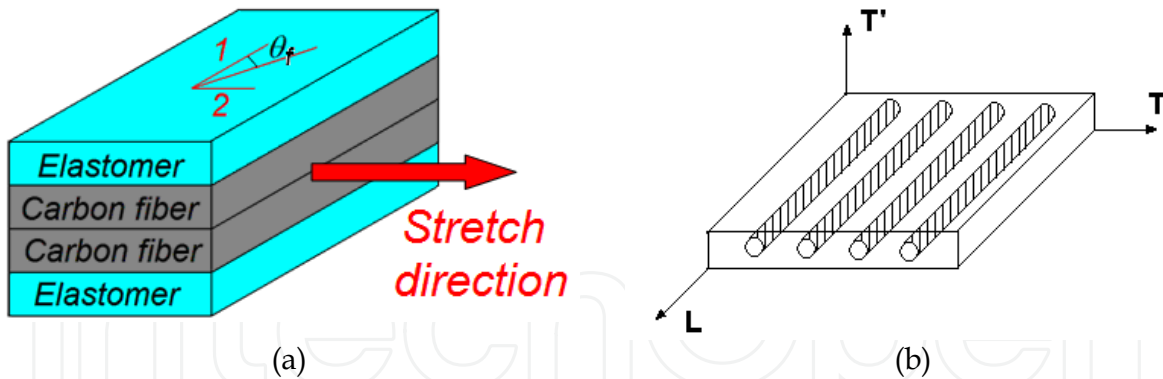


Fig. 4. (a) EMC lay-up used in CLPT predictions. (b) Unidirectional composite layer showing fiber orientation.

perfect bonding occurs between the fiber and matrix material such that equal strain is experienced by both fiber and matrix in the L direction. Based upon these assumptions, the longitudinal elastic modulus is given by the rule of mixtures:

$$E_L = E_f V_f + E_m (1 - V_f) \quad (1)$$

Here  $E_L$  is the longitudinal elastic modulus for the layer,  $E_f$  is the fiber elastic modulus,  $E_m$  is the matrix elastic modulus, and  $V_f$  is the fiber volume fraction. To find the elastic modulus in the transverse direction, it is assumed that stress is uniform through the matrix and fiber. The equation for the transverse modulus,  $E_T$ , is:

$$E_T = 1 / (V_f / E_f + (1 - V_f) / E_m) \quad (2)$$

Calculations based on these micromechanics assumptions supported the intuitive conclusion that thinner EMC skins would have a lower in-plane stiffness modulus in the spanwise direction,  $E_2$ . Predictions for the transverse elastic modulus and the minor Poisson's ratio are plotted versus fiber offset angle in Figure 5a and Figure 5b, respectively, as solid lines. In order to provide some validation for the CLPT predictions, three EMC sample coupons were manufactured, consisting of 0.5 mm elastomer face sheets sandwiching two 0.2-0.3 mm composite lamina with a fiber volume fraction of 0.7. Nominal fiber axis offset angles of  $0^\circ$ ,  $10^\circ$ , and  $20^\circ$  were used. The measured transverse modulus and minor Poisson's ratio are plotted as circles in their respective figure. As expected, increasing fiber offset angle increases the in-plane stiffness of the EMC, requiring greater actuation forces. Also, it is noteworthy that the inclusion of unidirectional fiber reinforcement at  $0^\circ$  offset angle nearly eliminates minor Poisson's ratio effects as predicted by CLPT theory.

It is of critical importance to note that, according to the assumptions used in deriving the lamina transverse modulus in Eq. (2), the transverse modulus has a lower bound equal to the matrix modulus. This lower bound is shown in Figure 5a as a horizontal black line at  $E_2/E_m = 1$ . However, the experimental data is close to this lower bound for the  $10^\circ$  and  $20^\circ$  samples, and the modulus is actually below the lower bound for the  $0^\circ$  case. Clearly in this case there is a problem in the micromechanics from which the transverse modulus prediction was derived.

Recall it was assumed that perfect bonding between fiber and matrix occurred, as illustrated in Figure 6a. This implies stress was equally shared between matrix and fiber under transverse loading. Close visual examination of the EMC samples during testing revealed that the fiber/matrix bond was actually very poor, and the matrix pulled away from individual fibers under transverse loading as illustrated in Figure 6b. Thus, the fibers carry no stress in the transverse direction, and the effective cross-sectional area of matrix left to carry transverse force in the lamina is reduced by the fiber volume fraction. For the case of poor transverse bonding exhibited in the fiber laminae, the transverse modulus in Eq. (2) can thus be simplified to:

$$E_T = E_m / (1 - V_f) \quad (3)$$

Using Eq. (3) to calculate transverse modulus for the fiber laminae, new CLPT predictions for EMC non-dimensionalized transverse modulus and minor Poisson's ratio are also plotted in Figure 5a and 5b, respectively. Much better agreement is seen between the analytical and experimental values for  $E_2/E_m$ . In spite of the poor bond between fiber and matrix material in the EMCs, the fiber stiffness still appears to contribute to the transverse stiffness at higher fiber offset angles. The minor Poisson's ratio is also influenced by the fiber offset angle. The EMC's longitudinal modulus, not shown, also remains high. These findings clearly indicate the fiber continues to contribute to the longitudinal stiffness of the fiber laminae even when bonding between matrix and fiber is poor.

To explain this contribution, it is hypothesized that friction between fiber and matrix help share load between the two materials in the longitudinal direction, while the matrix is free to pull away from the fiber in the transverse direction. This would explain the stiffening effect seen in the transverse modulus at increased offset angles and the controlling effect the fiber appears to have on Poisson's ratio at very low offset angles.

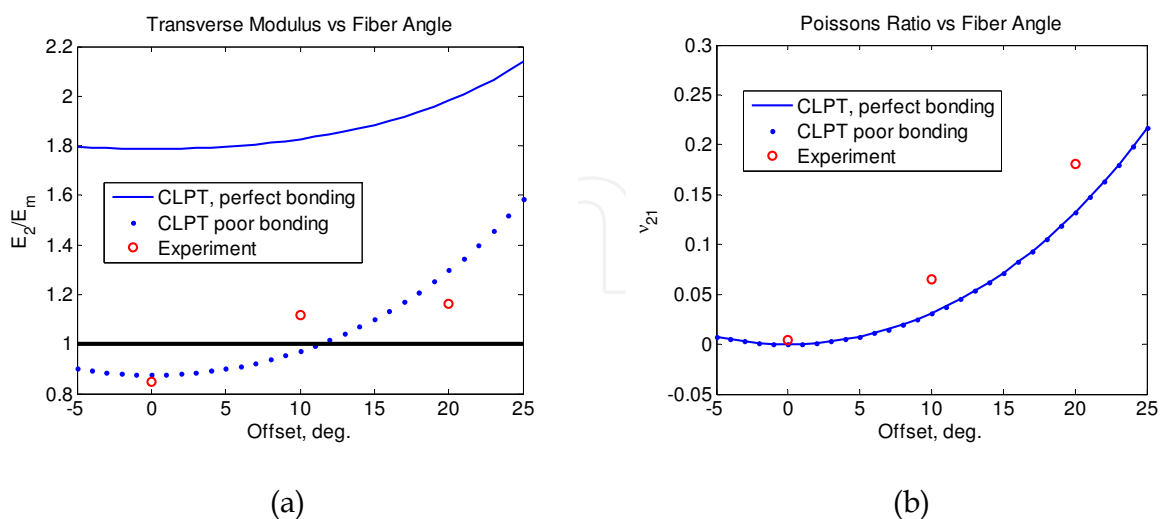


Fig. 5. Comparison of CLPT predictions with experimental data for three different fiber angles (a) non-dimensionalized transverse elastic modulus  $E_2/E_m$ , (b) minor Poisson's ratio  $\nu_{21}$ .



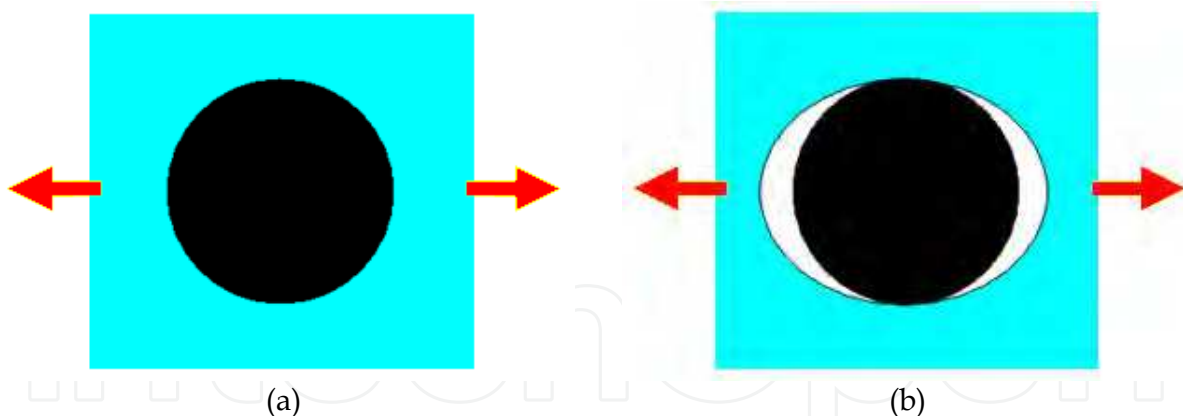


Fig. 6. Fiber/matrix bond (a) assumed perfect bonding and equal transverse stress sharing in CLPT, (b) actual condition with poor fiber/matrix bond and no fiber stress under transverse loading.

Based upon these CLPT results, a fiber offset angle of  $0^\circ$  was selected to minimize transverse stiffness and also to minimize the minor Poisson's ratio. As the analytical and experimental results in Figure 5b indicate, a  $0^\circ$  fiber offset angle can resist chordwise shape change during spanwise morphing. While this conclusion appears obvious, the results demonstrate that with the appropriate correction to micromechanics assumptions in the transverse direction, simple CLPT analysis can be more confidently used to predict EMC directional properties. This simplifies the morphing skin design procedure by allowing in-plane EMC stiffness to be predicted by analytical methods.

### 3.3 EMC fabrication and testing

A key issue in this study was developing a dependable and repeatable skin manufacturing process. The final manufacturing process involved a multi-step lay-up process, building the skin up through its thickness (Figure 7). First, a sheet of elastomer was cast between two aluminum caul plates using shim stock to enforce the desired thickness. Secondly, unidirectional carbon fiber was applied to the cured elastomer sheet, with particular attention paid to the alignment of the fibers to ensure that they maintained their uniform spacing and unidirectional orientation (or angular displacement, depending on the sample). Enough additional liquid elastomer was then spread on top of the carbon to wet out all of the fibers. An aluminum caul plate was placed on top of the lay-up, compressing the carbon/elastomer layer while the elastomer cured. The third and final step in the skin lay-up process was to build the skin up to its final thickness. The bottom sheet of skin with attached carbon fiber was laid out on a caul plate. As in the first step, shim stock was used to enforce the desired thickness (now the full thickness of the skin) and liquid elastomer was poured over the existing sheet. A caul plate was then placed on top of this uncured elastomer and left for at least 4 hours. Once cured, the completed skin was removed from the plates, trimmed of excess material, and inspected for flaws. A successfully manufactured skin had a consistent cross-section and no air bubbles or visible flaws.

Several EMC sheets were originally manufactured in an effort to experimentally test the effect of fiber thickness and orientation on in-plane and out-of-plane characteristics and to attempt to optimize both. Table 2 describes the nominal dimensions and fiber angle values

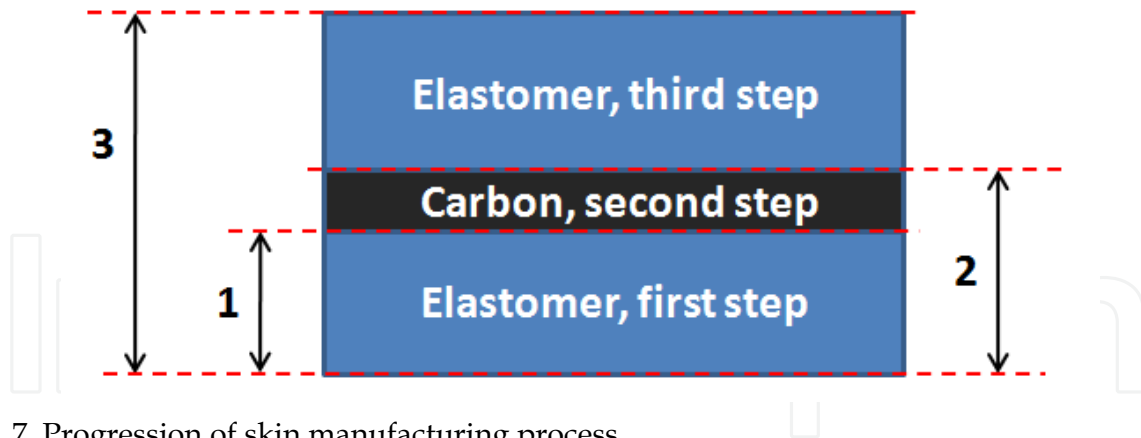


Fig. 7. Progression of skin manufacturing process.

for the three EMC samples. EMC #3 was not intended to be used in the final morphing skin demonstrator, but instead was an academic exercise intended to increase out-of-plane stiffness at the expense of in-plane stiffness.

|        | Sheet thickness (mm) | Fiber orientation (deg) | Fiber layer thickness (mm) | Total Thickness (mm) |
|--------|----------------------|-------------------------|----------------------------|----------------------|
| EMC #1 | 0.5                  | 0                       | 0.4                        | 1.4                  |
| EMC #2 | 0.5                  | 0                       | 0.7                        | 1.7                  |
| EMC #3 | 0.5                  | +15, 0, -15 deg         | 0.8                        | 1.8                  |

Table 2. Summary of EMC sample properties.

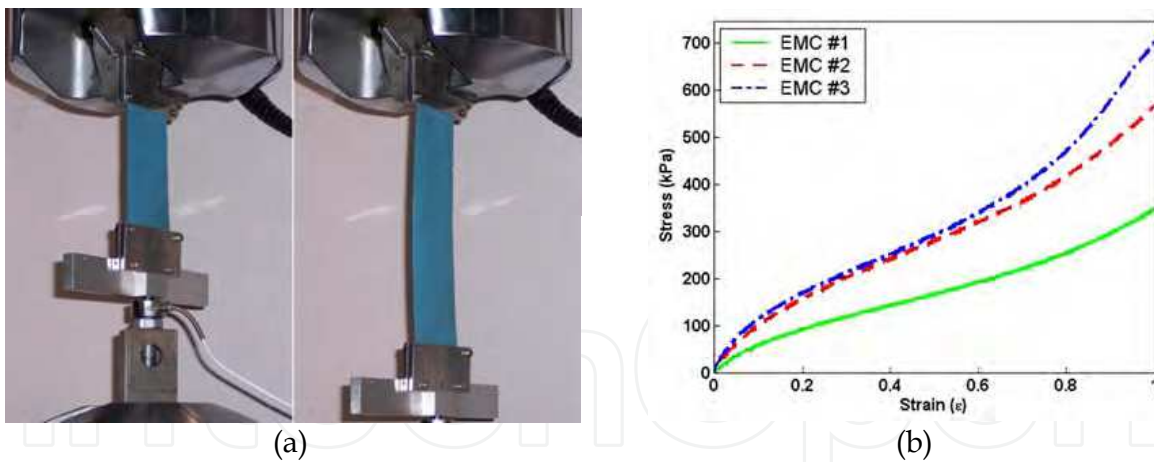


Fig. 8. In-plane skin testing, (a) EMC sample taken to 100% strain; (b) data from EMC samples.

Sample strips measuring 51 mm x 152 mm were cut from the three EMCs and tested on a Material Test System (MTS) machine. Each sample was strained to 100% of its original length and then returned to its resting position. The test setup is depicted in Figure 8a and data from these tests are presented in Figure 8b. Notice the visibly low Poisson’s ratio effects as the EMC is stretched to 100% strain in Figure 8a – there is little measurable reduction in width. It is also important to note that the stress-strain curves measured for each EMC reflect not only the impact of their lay-ups on stiffness, but also improvements in

manufacturing ability. Thus, due to improved control of carbon fiber angles and the thickness of elastomer matrix, EMC #3 has roughly the same stiffness as EMC #2, in spite of the larger amount of carbon fiber present and higher fiber angles. EMC #1 exhibited high quality control and linearity of fiber arrangement and has the lowest stiffness of all, regardless of its nominal similarity to EMC #2. Based upon these tests, EMC #1 and EMC #2 were selected for incorporation into integrated test articles. EMC #1 displayed the lowest in-plane stiffness, while EMC #2 had the second lowest stiffness, making them the most attractive candidates for a useful morphing skin.

#### 4. Substructure development

The most challenging aspect of the morphing skin to design was the substructure. Structural requirements necessitated high out-of-plane stiffness to help support the aerodynamic pressure load while still maintaining low in-plane stiffness and high strain capability.

##### 4.1 Honeycomb design

The substructure concept originally evolved from the use of honeycomb core reinforcement in composite structures such as rotor blades. Honeycomb structures are naturally suited for high out-of-plane stiffness, and if properly designed can have tailored in-plane stiffness as well (Gibson and Ashby, 1988). By modification of the arrangement of a cellular structure, the desired shape change properties can be incorporated.

In order to create a honeycomb structure with a Poisson's ratio of zero, a negative Poisson's ratio cellular design presented by Chavez *et al.* (2003), or so-called auxetic structure (Evans *et al.*, 1991), was rearranged to resemble a series of v-shaped members connecting parallel rib-like members, as seen in Figure 9. This arrangement gives large strains in one direction with no deflection at all in the other by means of extending or compressing the v-shaped members, which essentially act as spring elements. The chordwise rib members act as ribs in a conventional airplane wing by defining the shape of the EMC face sheet and supporting against out-of-plane loads. The v-shaped members connect the ribs into a single deformable substructure which can then be bonded to the EMC face sheet as a unit, with the v-shaped bending members controlling the rib spacing.

For a standard honeycomb, Gibson and Ashby (1988) describe the in-plane stiffness as a ratio of in-plane modulus to material modulus, given in terms of the geometric properties of the honeycomb cells. By modifying this standard equation, it is possible to describe the in-plane stiffness of a zero-Poisson honeycomb structure with cell geometric properties as illustrated in Figure 10a. Here  $t$  is the thickness of the bending (v-shaped) members,  $\ell$  is the length of the bending members,  $h$  is the cell height,  $c$  is the cell width, and  $\theta$  is the angle between the rib members and the bending members. Note that in the figure the cell is being stretched vertically and  $F$  is the force carried by a bending member under tension. Also note that the depth of the cell, denoted as  $b$ , is not represented in Figure 10.

With the geometry of the cell defined, an expression can be found for the honeycomb's equivalent of a stress-strain relationship. For small deflections, the bending member between points 1 and 2 can be considered an Euler-Bernoulli beam as shown in Figure 10b, with the forces causing a second mode deflection similar to a pure moment. From Euler-

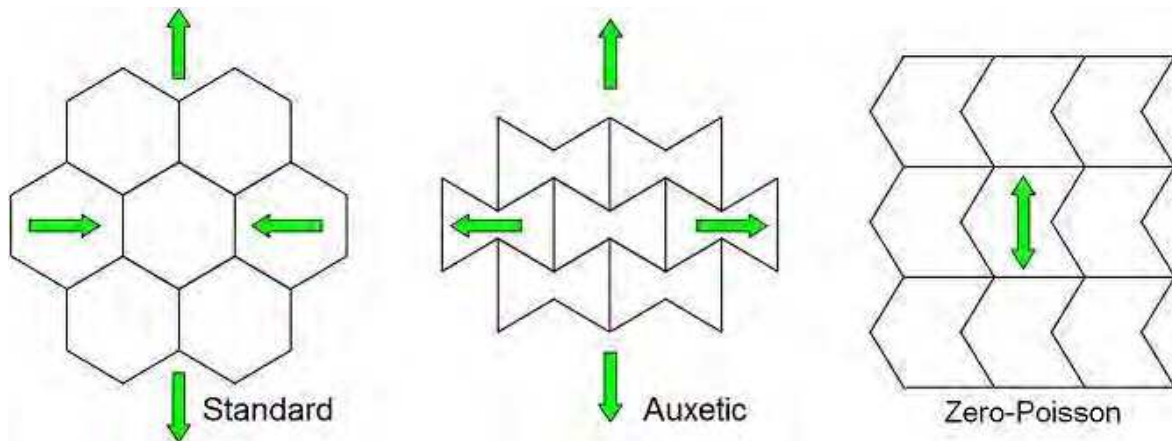


Fig. 9. Comparison of standard, auxetic, and modified zero-Poisson cellular structures showing strain relationships.

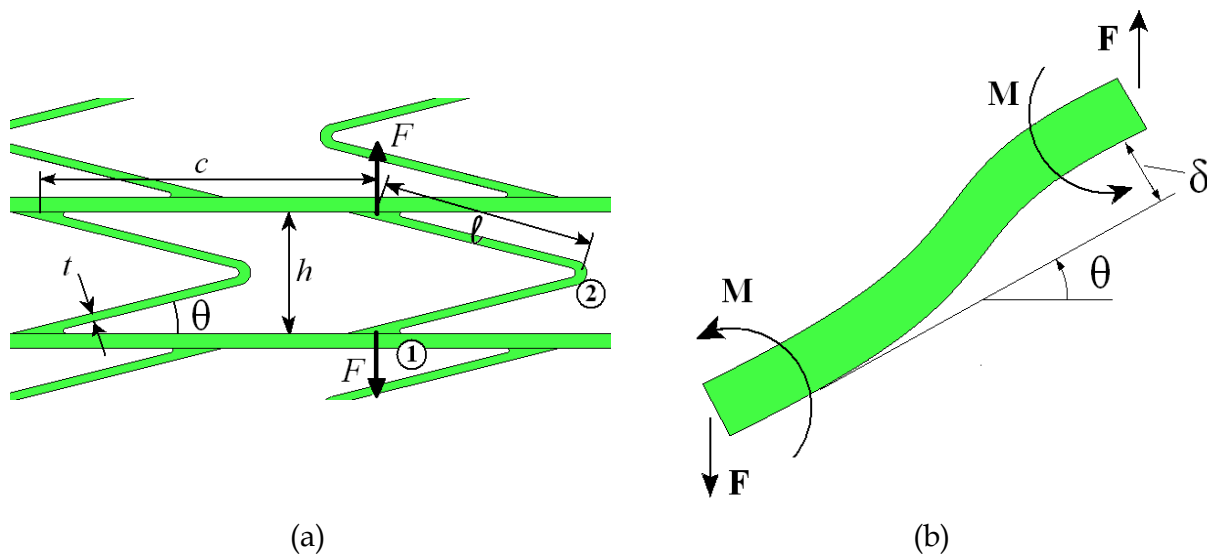


Fig. 10. (a) Geometry of zero-Poisson honeycomb cell, (b) Forces and moments on bending member leg.

Bernoulli theory, the cosine component of the force  $F$  will cause a bending deflection  $\delta$  (Shigley *et al.*, 2004):

$$\delta = \frac{F \cos \theta \ell^3}{12E_0I} \tag{4}$$

Here  $E_0$  is the Young’s Modulus of the honeycomb material and  $I$  is the second moment of the area of the bending member; in this case  $I = bt^3/12$ . In order to determine an effective tensile modulus for the honeycomb substructure, the relationship in Eq. (4) between force and displacement needs to be transformed into an equivalent stress-strain relationship. The equivalent stress through one cell can be found by using the cell width  $c$  and honeycomb depth  $b$  to establish a reference area, and the global equivalent strain is determined by non-dimensionalizing the v-shaped member’s bending deflection  $2\delta$  by the cell height  $h$ . These

equivalent stresses and strains are used to determine a transverse stiffness modulus for the honeycomb,  $E_2$ :

$$\sigma_2 = \frac{F}{cb}, \quad (5)$$

$$\varepsilon_2 = \frac{\delta \cos \theta}{h/2}, \quad (6)$$

$$E_2 = \frac{\sigma_2}{\varepsilon_2} \quad (7)$$

Substituting Eqns. (5) through (7) into Eq. (4) and simplifying yields the following expression for the stiffness of the overall honeycomb relative to the material modulus:

$$\frac{E_2}{E_0} = \left(\frac{t}{l}\right)^3 \frac{\sin \theta}{\frac{c}{l} \cos^2 \theta} \quad (8)$$

Because this modified Gibson-Ashby model assumes the bending member legs to be beams with low deflection angles and low local strains, Eq. (8) should only be valid for global strains that result in small local deflections. However, it will be shown that due to the nature of the honeycomb design, relatively large global strains are achievable with only small local strains.

With this fairly simple equation, the cell design parameters can easily be varied and their effect on the overall in-plane stiffness of the structure can be studied. For fixed values of  $t$ ,  $h$ ,  $c$ , and  $b$ , the modulus ratio of the structure,  $E_2/E_0$ , increases with the angle  $\theta$ . Noting the definitions in Figure 10a, it can be seen that decreasing  $\theta$  consequently affects the bending member length  $l$ , as the upper and lower ends must meet to form a viable structure. Thus, for a given cell height  $h$ , minimum stiffness limitations are introduced into the design from a practicality standpoint in that the bending members must connect to the structure and cannot intersect one another. Lower in-plane stiffness can be achieved by increasing cell width to accommodate lower bending member angles.

In Figure 11a, an example is given of a zero-Poisson substructure designed in a commercial CAD software and produced on a rapid prototyping machine out of a photocure polymer. Using this method, a large number of samples could be fabricated with variations in bending member angle,  $\theta$ . By testing these structures on an MTS machine (Figure 11b), a comparison could be made between the predicted effect of bending member angle on in-plane stiffness and the actual observed effect.

The stress-strain test data from a series of rapid prototyped honeycombs is presented in Figure 12a. Each honeycomb was tested over the intended operating range, starting at a reference length of 67% of resting length (pre-compressed) and extending to 133% of resting length to achieve 100% total length change. To test the validity of the modified Gibson-Ashby model, comparisons of experimental data and analytical predictions were made. The stiffness modulus of each experimentally tested honeycomb was determined by applying a

linear least squares regression to the data in Figure 12a. The resulting stiffnesses were then plotted with the analytical predictions from Eq. (8) in Figure 12b.

The strong correlation between the analytical predictions and measured behaviour suggests the assumptions made in the modified Gibson-Ashby equation are accurate over the intended operating range of the honeycomb substructure, and local strains are indeed relatively low. Having low local strain is a benefit as it will increase the fatigue life of the substructure. The low local strains were verified with a finite element analysis that predicted a maximum local strain of 1.5% while undergoing 30% compression globally, a 20:1 ratio. This offers hope that a honeycomb substructure capable of high global strains with a long fatigue life can be designed by minimizing local strain, an area which should be a topic of further research. Further details regarding this structure can be found by consulting Kothera *et al.* (2011).



Fig. 11. (a) Example of Objet PolyJet rapid-prototyped zero-Poisson honeycomb, (b) morphing substructure on MTS machine.

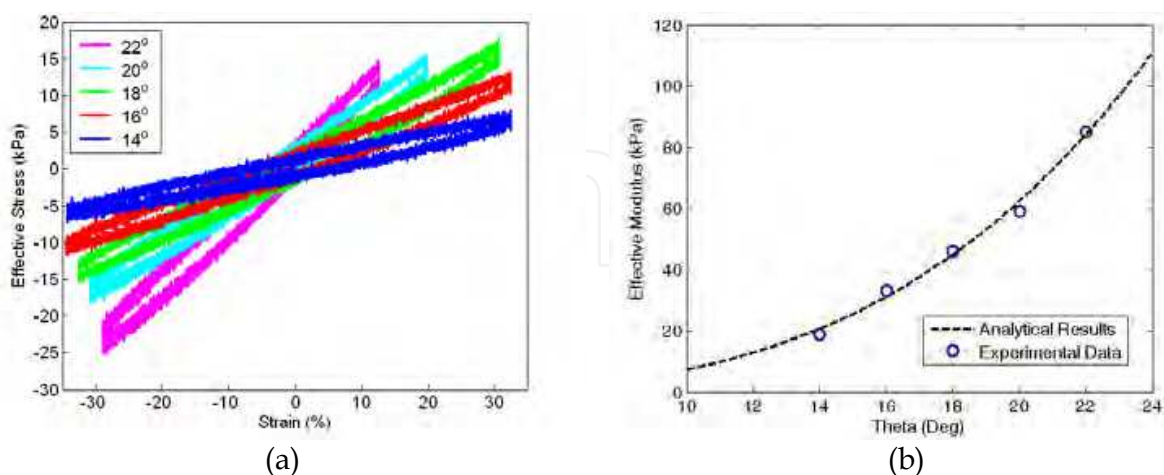


Fig. 12. (a) Stress-strain curves of substructures of various interior angles, (b) In-plane substructure stiffness, analytical versus experiment.

To minimize the in-plane stiffness of the substructure, the lowest manufacturable bending member angle,  $14^\circ$ , was selected for integration into complete morphing skin prototypes.

Furthermore, this testing demonstrated the usefulness of the modified Gibson-Ashby equation for future honeycomb substructure design efforts. The in-plane stiffness of zero-Poisson honeycomb structures can be predicted.

## **5. One dimensional morphing demonstrator**

### **5.1 Carbon fiber stringers**

One unfortunate aspect of the zero-Poisson honeycomb described above is the lack of bending stiffness about the in-plane axis perpendicular to the rib members. Another structural element is needed to reinforce the substructure for out-of-plane loads. In order to reinforce the substructure, carbon fiber “stringers” were added perpendicular to the rib members. Simply comprised of carbon fiber rods sliding into holes in the substructure, the stringers reinforce the honeycomb against bending about the transverse axis.

The impact of the stringers on the in-plane stiffness of the combined skin was imperceptible. Fit of the stringer through the holes in the substructure was loose and thus the assembly had low friction. Additionally, the EMC sheet and bending members of the substructure kept the substructure ribs stable and vertical, preventing any binding while sliding along the stringers.

### **5.2 EMC/substructure adhesive**

In order to integrate the EMC face sheets with the honeycomb substructure and carry in-plane loads, a suitable bonding agent was necessary. The desired adhesive was required to bond the silicone EMC to the plastic rapid-prototyped honeycomb sufficiently to withstand the shear forces generated while deforming the structure. In addition, the adhesive also needed to be capable of high strain levels in order to match the local strain of the EMC at the bond site. Loads imposed on the adhesive by distributed loads (such as aerodynamic loads on the upper surface of a wing) were not taken into account in this preliminary study.

Due to the fact that the substructure, and not the EMC itself, would be attached to the actuation mechanism, the adhesive was required to transfer all the force necessary to strain the EMC sheet. Based upon the known stiffness of the EMCs selected for integration into the morphing skin prototype, the adhesive was required to withstand up to 10.5 N/cm of skin width for 100% area change. The adhesive was to bond the EMC along a strip of plastic 2.54 cm deep, so the equivalent shear strength required was 41.4 kPa. A couple silicone-based candidate adhesives were selected for lap shear evaluation, all of which were capable of high levels of strain. Test results indicated that Dow Corning (DC) 700, Industrial Grade Silicone Sealant, a one-part silicone rubber that is resistant to weathering and withstands temperature extremes, was most capable of bonding the EMC skin to the substructure, as it had a safety factor of 2.

### **5.3 Morphing structure assembly**

A 152 mm x 152 mm morphing skin sample was fabricated from EMC #1. A 14° angle honeycomb was used for the substructure, and DC 700 adhesive was used to bond the EMC to the honeycomb substructure. To assist in the attachment, the rib members of the

honeycomb core were designed with raised edges on one side, as shown in Figure 13a. This figure shows a side view of the zero-Poisson honeycomb, where it can be seen that the top surface has the ribs extended taller than the bending members. Therefore, the bonding layer can be applied to the raised rib surfaces and pressed onto the EMC without bonding the bending members to the EMC. A sectional side view of a single honeycomb cell, shown in Figure 13b, illustrates conceptually how the bonded morphing skin looks. A thin layer of adhesive is shown between the EMC and the ribs of the honeycomb, but it does not affect the movement of the bending members. The outermost two ribs on the substructure were each 26 mm wide, providing large bonding areas to carry the load of the skin under strain. This left 100 mm of active length capable of undergoing high strain deformation.



Fig. 13. EMC-structure bonding method – (a) honeycomb core; (b) single cell diagram.

The configuration of the morphing skin design is summarized in Table 3. The assembled morphing skin sample was used to assess in-plane and out-of-plane stiffness before fabricating a final 165 mm x 330 mm full scale test article for combination and evaluation with the PAM actuation system described in Section 2.

| EMC                                       | Honeycomb                                  | Adhesive | Active Length |
|---|--|----------|---------------|
| EMC #1, 1.4 mm thick, two CF layers at 0° | 14° zero-Poisson rapid prototyped VeroBlue | DC-700   | 100 mm        |

Table 3. Morphing skin configuration.

#### 5.4 In-plane testing

The morphing skin sample was tested on an MTS machine to 50% strain. The level of strain was limited in order to prevent unforeseen damage to the morphing skin before it could be tested for out-of-plane stiffness as well. In Figure 14a, the morphing skin is shown undergoing in-plane testing, with results presented in Figure 14b. Note that the test procedure strained the specimen incrementally to measure quasi-static stiffness, holding the position briefly before starting with the next stage. Relaxation of the EMC sheet is the cause for the dips in force seen in the figure.

Based upon the individually measured stiffnesses of the EMC and substructure components used in the morphing skin and the stiffness of the skin overall, the energy required to strain each structural element can be determined (Figure 15), with the adhesive strain energy found by subtracting the strain energy of the other two components from the total for the morphing skin. The strain energy contribution of each element is broken down in energy per unit width required to strain the sample from 10 cm to 20 cm.



It can be seen that the adhesive had a considerable strain energy requirement, more than double that of the honeycomb substructure. When designing future morphing skins, the energy to strain the adhesive layer must be taken into account to ensure sufficient actuation force is available to meet strain requirements. More careful attention to minimizing the amount of adhesive used to bond the skin and substructure would also likely reduce the in-plane stiffness of the morphing skin by a non-trivial amount.

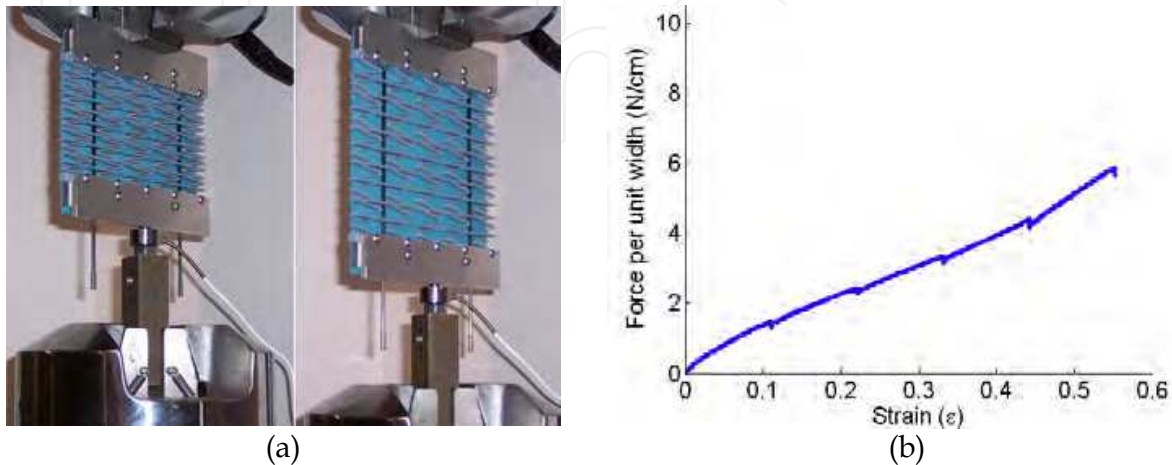


Fig. 14. Morphing skin sample in-plane testing – (a) Skin #1 on MTS; (b) Data from morphing skin in-plane testing.

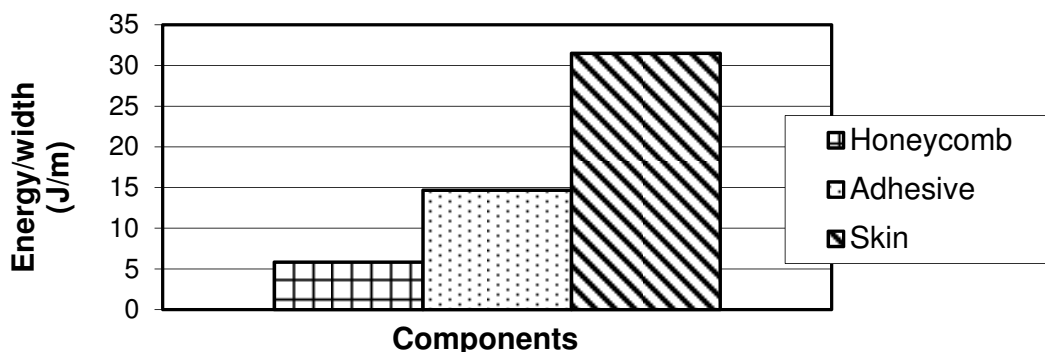


Fig. 15. Contributions to morphing skin strain energy.

### 5.5 Out-of-plane testing

The final phase of evaluation for morphing skin sample required measuring out-of-plane deflection under distributed loadings, approximating aerodynamic forces. A number of testing protocols were investigated, including ASTM standard D 6416/D 6416M for testing simply supported composite plates subject to a distributed load. This particular test protocol is intended for very stiff composites, not flexible or membrane-like composites. A simpler approach to the problem was adopted wherein acrylic retaining walls were placed above the morphing skin sample into which a distributed load of lead shot and sand could be poured. The final configuration of the out-of-plane deflection testing apparatus can be seen in Figure 16a. A set of lead-screws stretched the morphing skin sample from rest to 100% strain. The acrylic retaining walls could be adjusted to match the active skin area, and were tall enough to contain lead shot equivalent to a distributed load of 200 psf (9.58 kPa). By applying a thin

layer of sand directly to the surface of the skin, the weight of the lead shot was distributed relatively evenly over the surface of the EMC. Moreover, as the skin deflected under load, the sand would adjust to conform to the surface and continue to spread the weight of the lead. A single-point laser position sensor was also placed underneath to measure the maximum deflections at the center of the skin, between the rib members.

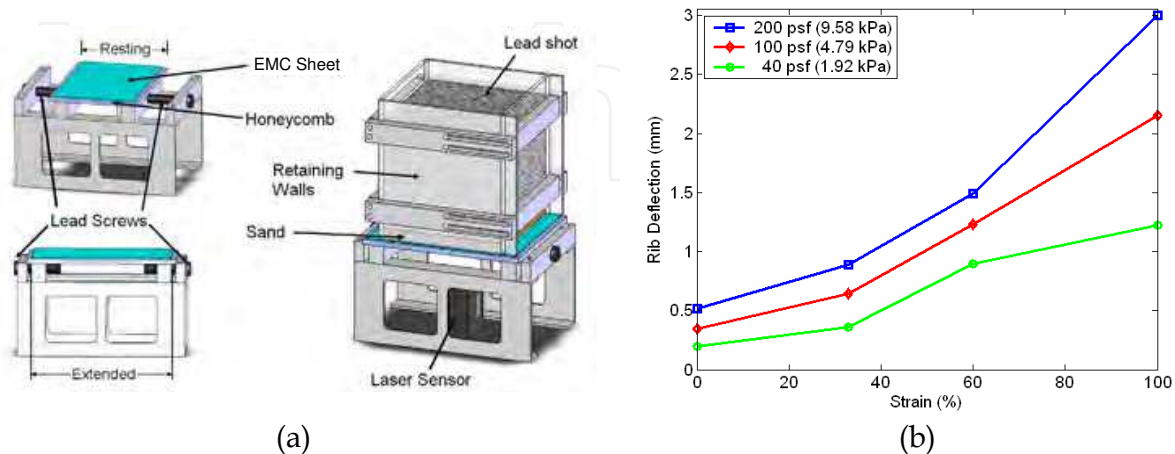


Fig. 16. (a) Out-of-plane deflection test apparatus design. (b) Out-of-plane deflection results as measured on the center rib.

The test procedure for each morphing skin covered the full range of operation, from resting (neutral position) to 100% area change. Lead-screws were used to set the skin to a nominal strain condition between 0% and 100% of the resting length. The laser position sensor shown below the skin in the figure was positioned in the center of a honeycomb cell at the center of the morphing skin, where the greatest deflection is seen. This positioning was achieved using a small two-axis adjustable table. The laser was zeroed on the under-surface of the EMC, and the relative distance to the bottom of an adjacent rib was measured. This established a zero measurement for rib deflection as well. A layer of sand with known weight was poured onto the surface of the EMC, and lead shot sufficient to load the skin to one of the three desired distributed loads was added to the top of the sand. Wing loadings of 40 psf (1.92 kPa), 100 psf (4.79 kPa), and 200 psf (1.92 kPa) were simulated. Once the load had been applied, measurements were taken at the same points on the EMC and the adjacent rib to determine deflection. These measurements were repeated for four different strain conditions (0, 25%, 66%, 100%) and the three different noted distributed loads.

Experimental results from the morphing skins is provided in Figure 16b. It was observed that, relative to the rib deflections, the EMC sheet itself deflected very little (less than 0.25 mm). The results therefore ignore the small EMC deflections and show only the maximum deflection measured on the rib at the midpoint of each morphing skin. Overall, the morphing skin deflections show that as the skin is strained and unsupported length increases, the out-of-plane deflection increases. Naturally, the deflection increases with load as well. Based on observation and on these results, the EMC sheets appeared to carry a greater out-of-plane load than expected, probably due to tension in the skin. EMC deflections between ribs remained low at all loading and strain conditions, while the substructure experienced deflections an order of magnitude greater. Future iterations of morphing skins will require stiffer substructures to withstand out-of-plane loads.

### 5.6 Full scale integration and evaluation

After proving capable of reaching over 100% strain with largely acceptable out-of-plane performance, the morphing skin sample from the previous subsection was used as the basis for a larger test article. A 34.3 cm x 14 cm morphing skin, nominally identical to the morphing skin sample in configuration, was fabricated and attached to the actuation assembly. The actuation assembly, honeycomb substructure, and completed morphing cell can be seen in Figure 17. Individual components of the system are pictured in Figure 17a, while the assembled morphing skin test article appears in Figure 17b. The active region stretches from 9.1 cm to 18.3 cm with no transverse contraction, thus, producing a 1-D, 100% increase in surface area with zero Poisson's ratio.

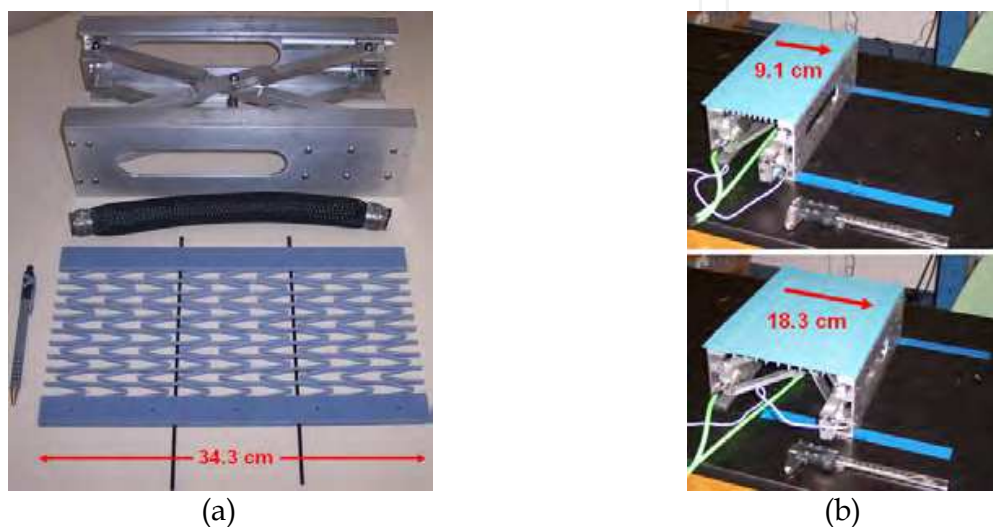


Fig. 17. Integration of morphing cell – (a) actuation and substructure components; (b) complete morphing cell exhibiting 100% area change.

To characterize the static performance of the morphing cell, input pressure to the PAM actuators was increased incrementally and the strain of the active region was recorded at each input pressure, and a load cell in line with one PAM recorded actuator force for comparison to predicted values. This measurement process was repeated three times, recording strain, input pressure, and actuator force at each point. Note that the entire upper surface of the EMC is not the active region: each of the fixed-length ends of the honeycomb was designed and manufactured with 25.4 mm of excess material to allow adequate EMC bonding area and an attachment point to the mechanism. This inactive region can be seen on the top and bottom of the honeycomb shown in Figure 17a. The two extremities of the arrows in Figure 17b also account for the inactive region at both ends of the morphing skin.

The static strain response to input actuator pressure is displayed in Figure 18. Strain is seen to level off with increasing pressure due to a combination of mechanism kinematics and the PAM actuator characteristics, but the system was measured to achieve 100% strain with the PAMs pressurized to slightly over 620 kPa.

The measured system performance matches analytical predictions very closely. The previously mentioned analytical predictions and associated experimental data for the actuation system and skin performance are also repeated in this figure. The morphing cell

performance data, while not perfectly linear, approximately matches the slope of the experimental skin stiffness and intersects the actuation system experimental data near 100% extension. Furthermore, although the performance data falls roughly 15% short of original predictions, the morphing skin meets the design goal, validating the analytical design process. Losses were not included in the original system predictions. However, the margin of error included in the original design for friction, increased skin stiffness, and other losses enabled the final morphing cell prototype to achieve 100% strain. It should also be noted that 100% area increases could be achieved repeatedly at 1 Hz using manual actuator pressurization.

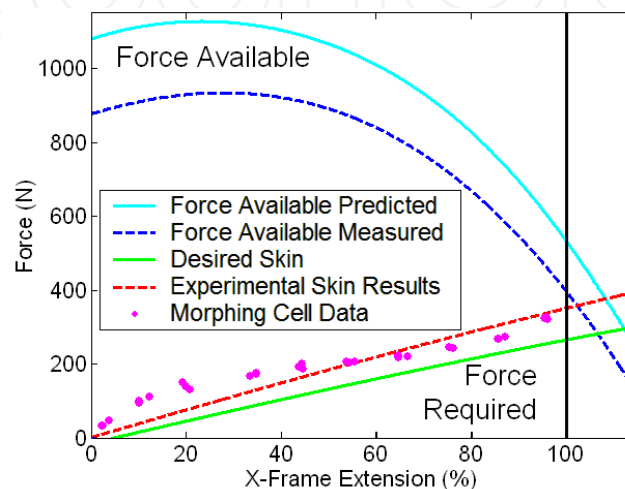


Fig. 18. Morphing cell data comparison with predictions.

## 6. Wind tunnel prototype

Building on the success of the 1-D morphing demonstrator, a wind tunnel-ready morphing wing was designed and tested. A key technical issue addressed here was determining the scalability of the skin and substructure manufacturing processes for use on a real UAV. Thus, the prototype airfoil system was designed such that future integration with a candidate UAV is feasible, and experimentally evaluated as a wind tunnel prototype. Nominal design parameters for the prototype are a 30.5 cm chord wing section capable of 100% span extension over a 61.0 cm active morphing section with less than 2.54 mm of out-of-plane deflection between ribs due to dynamic pressures consistent with a 130 kph maximum speed.

### 6.1 Structure development

Initially, the planar core design was extruded and cut into the form of a NACA 63<sub>3</sub>-618 airfoil with a chord of approximately 30.5 cm and span of 91.4 cm. A segment of the resulting morphing airfoil core appears in Figure 19a. While this morphing structure is capable of achieving greater than 100% length change itself, it has insufficient spanwise bending and torsional stiffness and so does not constitute a viable wing structure. The structure was therefore augmented with continuous sliding spars. Additionally, the center of the wing structure was hollowed out to potentially accommodate an actuation system for the span extension.

The final form of the morphing airfoil core is shown in Figure 19b. This figure shows a shell-like section mostly around the center of the airfoil, where an actuator could be located. Both the leading and trailing edges feature circular cut-outs to accommodate the carbon fiber spars, and near the trailing edge is a solid thickness airfoil shape for more rigidity where the airfoil is thinnest. The spars were sized using simple Euler-Bernoulli beam approximations and a desired tip deflection of less than 6.4 mm at full extension.

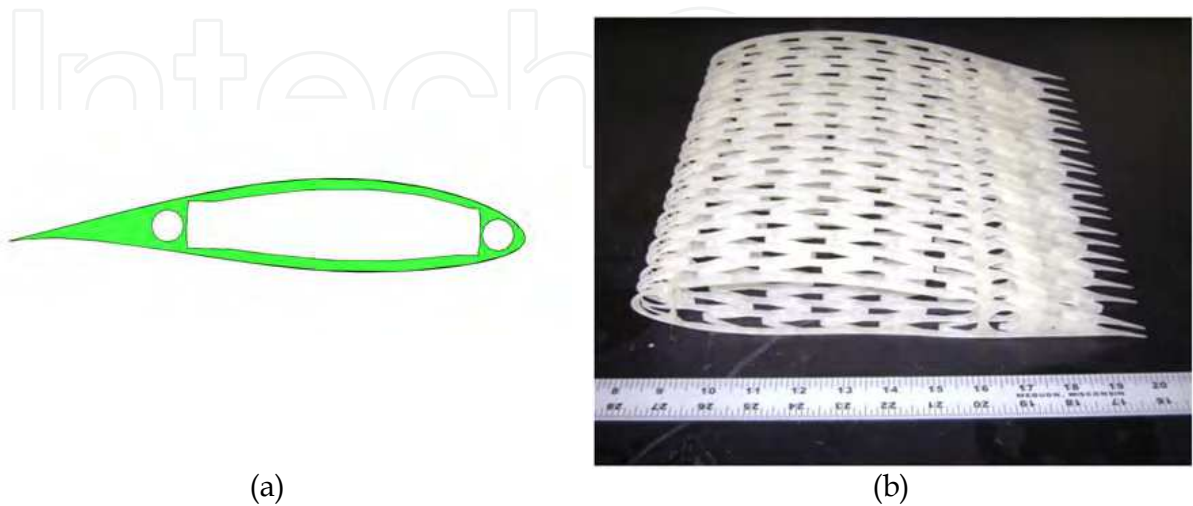
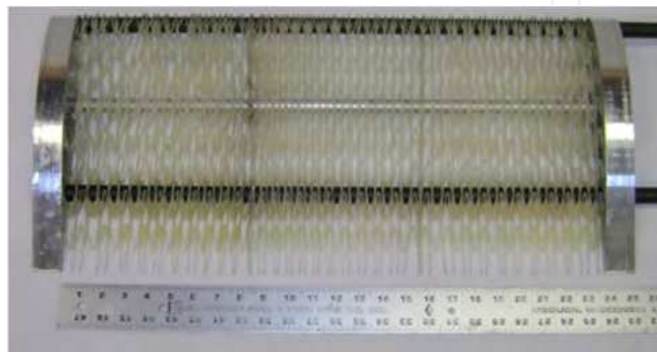


Fig. 19. (a) Final substructure design, cross-section view (b) Manufactured substructure, side view.

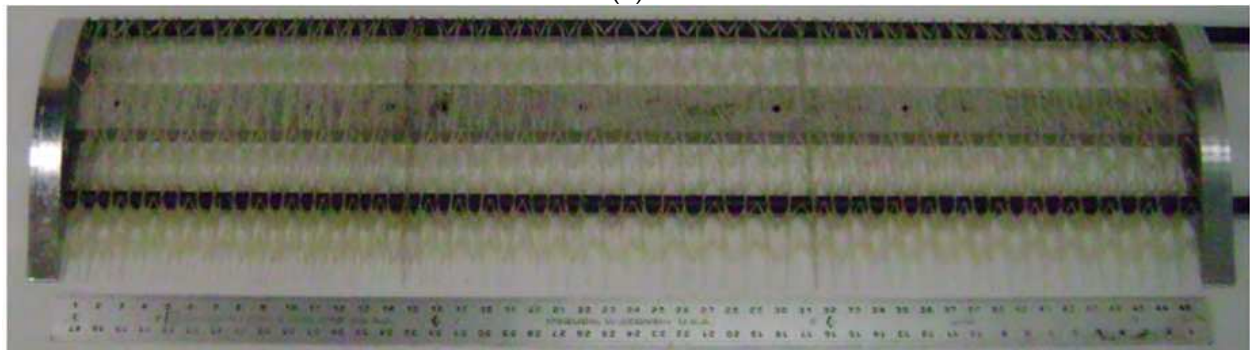
Due to the complex geometry of the morphing core and the desire for rapid part turn around, a stereo lithographic rapid-prototyping machine was again used to manufacture the morphing core sections from an acrylic-based photopolymer. The viability of this approach for flyable aircraft applications would have to be studied, but the material/manufacturing approach was sufficient for this proof-of-concept structural demonstrator. Other fabrication techniques such as investment casting, electrical discharge machining, etc. could be considered when fabricating this structure to meet full scale aircraft requirements. It should also be noted that the prototype will feature three of the core segments shown in Figure 19b. They will be pre-compressed when the EMC skin is bonded to allow for more expansion capability and introduce a nominal amount of tension in the EMC skin.

Figure 20a shows the core sections together between two aluminum end plates, with the leading edge and trailing edge support spars. The end plates were sized to provide a suitably large bonding surface for attaching the skin on the tip and root of the morphing section. In this configuration, the core sections are initially contracted such that the active span length is 61.0 cm. In terms of the aircraft, this contracted state will be considered the neutral, resting state because the EMC skin will not be stretched here and a potential actuation system would not be engaged. Hence, this is the condition in which the skin would be bonded to the core. Also shown in Figure 20b is the same arrangement in the fully extended (100% span increase) state with a span of 122.0 cm. The figure shows that the spacing between each of the rib-like members has nearly doubled from what was shown in the contracted state. This figure helps illustrate the large area morphing potential of this technological development in a way that could not be seen once the skin was attached.

Spanwise bending and torsional stiffness was provided by two 1.91 cm diameter carbon fiber spars. The spars were anchored at the leftmost outboard portion of the wing but were free to slide through the inboard end plates, thus allowing the wing to extend while maintaining structural integrity. The spars were sized in bending to deflect less than 2.54 cm at 100% extension under the maximum expected aerodynamic loads. Note that the spars are also capable of resolving torsional pitching moments, but as the express purpose of the present work was to demonstrate the feasibility of a span morphing wing, these torsional properties were not directly evaluated.



(a)



(b)

Fig. 20. Assembled core with spars and end plates – (a) contracted state; (b) extended state.

## 6.2 Prototype integration

The skin was bonded to the morphing substructure using DC-700. The skin was attached to each rib member, but not to the v-shaped bending members. Particular caution was used when bonding the skin to the end plates, as all of the tensile stress in the skin was resolved through its connection to the end plates.

At the resting condition with no elastic energy stored in the skin, Figure 21 shows the 0% morphing state with a 61.0 cm span. Increasing the span by another 61.0 cm highlights the full potential of this morphing system as the prototype wing section doubles its initial span, which has gone from 61.0 cm to 122 cm to show the 100% morphing capability (Figure 21b). Recall from the design that the wing section chord stays constant during these span

extensions, so the morphing percentages indicated (e.g., 100%) are consistent with the increase in wing area. As a fixed point of reference in each of these figures, note that the length of the white poster board underneath the prototype wing section does not change. Note also that this demonstration will use fixed-length internal spreader bars to hold the structure in different morphing lengths. Actuation was achieved by manually stretching the skin/core structure and then attaching the appropriate spreader bar to maintain the stretched distance.

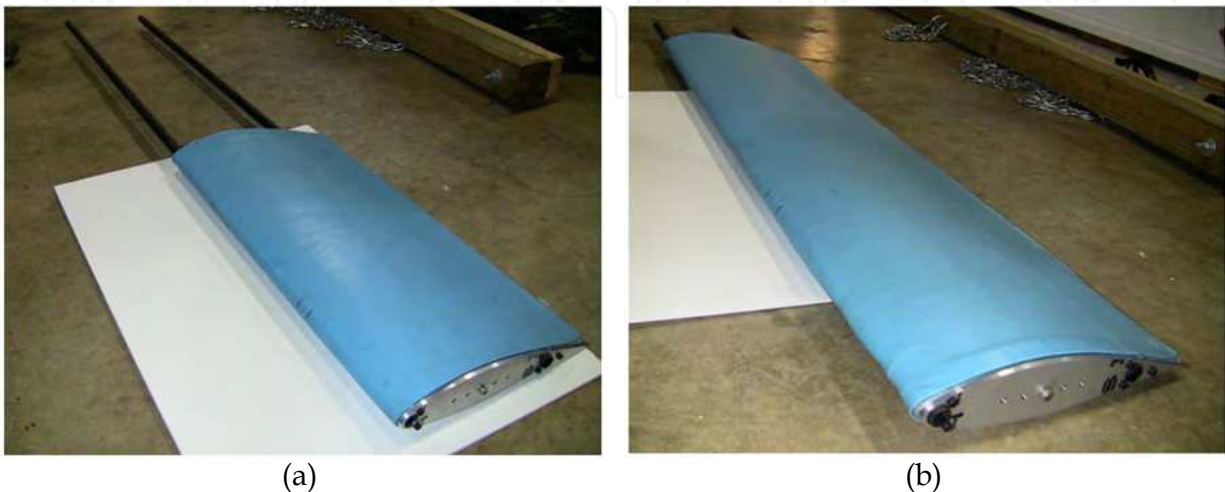


Fig. 21. Prototype morphing wing demonstration – (a) resting length, 0% morphing; (b) 61.0 cm span extension, 100% morphing.

### 6.3 Wind tunnel testing

Having shown that the prototype morphing wing section could achieve the goal of 100% span morphing for a total 100% wing area increase, the final test that was performed placed the wing section in a wind tunnel. The purpose of this test was to ensure that the EMC skin and core could maintain a viable airfoil shape at different morphing states under true aerodynamic loading, with minimal out-of-plane deflection between ribs. An open circuit wind tunnel at the University of Maryland with a 50.8 cm tall, 71.1 cm wide test section was used in this test. An overall view of the test section is shown in Figure 22a, with the wing at its extended length, and a close-up view of the test section is shown in Figure 22b looking upstream from the trailing edge.

With only a 50.8 cm tall test section in the wind tunnel, where only this span length of the prototype morphing wing would be placed in the wind flow, while the remaining span and support structure was below the tunnel. This is illustrated in Figure 22a, where the full extension condition (100% morphing) is shown. It should also be noted that while only a 50.8 cm span section of the wing is in the air flow, this is sufficient to determine whether or not the skin and core can maintain a viable airfoil shape in the presence of representative aerodynamic conditions, which was the primary goal of this test. That is, the morphing core motion and skin stretching is consistent and substantially uniform across the span of the prototype, so any characteristics seen in one small section of the wing could similarly be seen or expected elsewhere in the wing, making this 50.8 cm span “sampling” a reasonable measure of system performance.

Both the cruise (105 kph) and maximum (130 kph) rated speeds of the candidate UAV were tested. Three angles-of-attack ( $0^\circ$ ,  $2^\circ$ ,  $4^\circ$ ) and three wing span morphing conditions (0%, 50%, 100%) were also included in the test matrix. Tests were performed by first setting the morphing condition of the wing section, then positioning the wing for the desired angle-of-attack (AOA). With these values fixed, the tunnel was turned on and the speed was increased incrementally, stopping at the two noted test speeds while experimental observations were made. Tests were completed at each of the conditions in the table indicated with an x-mark. Note that tests were not performed at two of the angles-of-attack at the 100% morphing condition. This was because the skin began to debond near the trailing edge at one of the end plates. This occurred over a section approximately 7.6 cm in span at the 100% morphing condition, though the majority of the prototype remained intact. After removing the wing section from the wind tunnel and inspecting the debonded corner, it was discovered that very little adhesive was on the skin, core, and end plate. Thus, the likely cause for this particular debonding was inconsistent surface preparation, which can easily be rectified in future refinements. Note that the upper surface of the trailing edge experiences relatively small dynamic pressures compared to the rest of the wing, so that this debonding was most likely unrelated to the wind tunnel test. Rather, it was the result of manufacturing inconsistency.

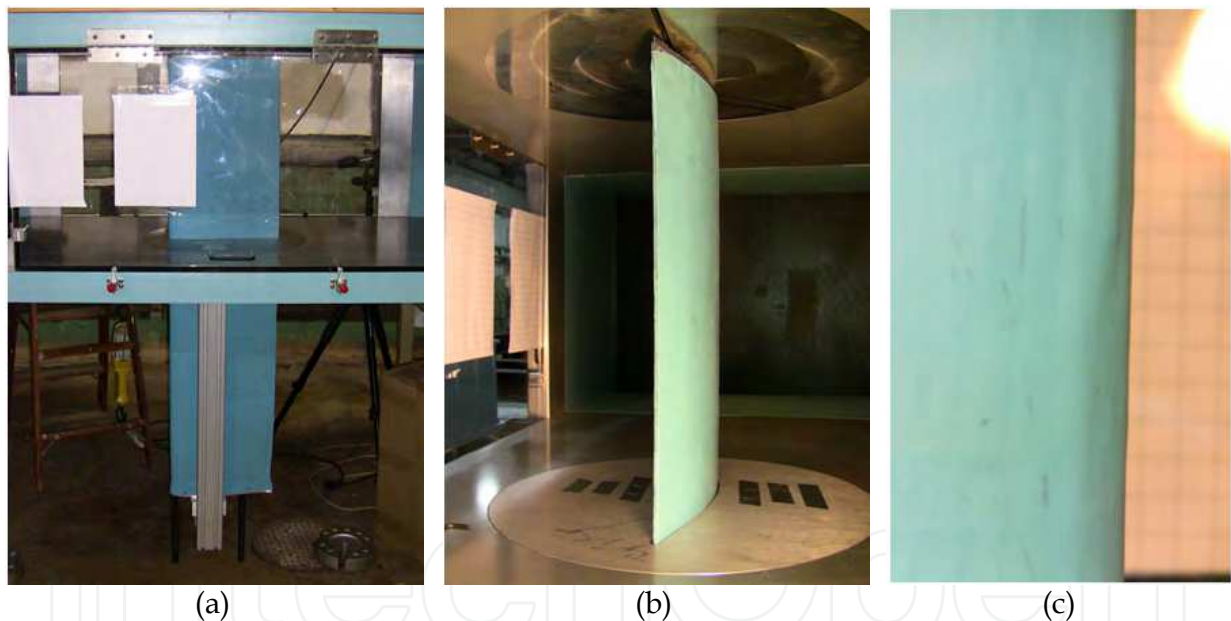


Fig. 22. Wind tunnel test setup - (a) Overall wind tunnel setup at 100% morphing; (b) Wing installed in wind tunnel - from trailing edge; (c) Picture of wing section leading edge at 130 kph, 100% morphing.

During execution of the test matrix, digital photographs (Figure 22c) were taken of the leading edge at each test point to determine the amount of skin deflection (e.g., dimpling) that resulted from the dynamic pressure. The leading edge location was chosen as the point to measure because the pressure is highest at the stagnation point. Pictures were taken perpendicular to the air flow direction and angled from the trailing edge, looking forward on the upper skin surface. Grids were taped to the outside of the transparent wall on the opposite side of the test section to provide reference lengths for processing. The



grids form 12.7 mm squares and are located 35.6 cm behind the airfoil in the frame of view, which is also 35.6 cm from the camera lens. These can be seen in Figure 22c. Using image processing, the maximum error in the measurements was determined to be  $\pm 7\%$ . This error can be attributed to vibration of the wind tunnel wall, which the camera lens was pressed against, or deviations in the focus of the pictures. In all the data processed, the maximum discernible out-of-plane deflection was approximately  $0.51 \pm 0.04$  mm, which is well within the goal of less than 2.54 mm. In reference to the 30.5 cm chord and 5.49 cm thickness, this deflection accounts for only 0.17% and 0.93%, respectively. Additionally, in observing this experiment, it can be qualitatively stated the morphing wing held its shape remarkably well under all tested conditions. This can be confirmed through visual inspection of the figures, as well.

## 7. Conclusions

This work explored the development of a continuous one dimensional morphing structure. For an aircraft, continuous morphing wing surfaces have the capability to improve efficiency in multiple flight regimes. However, material limitations and excessive complexity have generally prevented morphing concepts from being practical. Thus, the goal of the present work was to design a simple morphing system capable of being scaled to UAV or full scale aircraft. To this end, a passive 1-D morphing skin was designed, consisting of an elastomer matrix composite (EMC) skin with a zero-Poisson honeycomb substructure intended to support out-of-plane loads. In-plane stiffness was controlled to match the capabilities of an actuator by careful design and testing of each separate skin component. Complete morphing skins were tested for in-plane and out-of-plane performance and integrated with the actuator to validate the design process on a small-scale morphing cell section.

Design goals of 100% global strain and 100% area change were demonstrated on a laboratory prototype using the combined morphing skin and actuation mechanism. The morphing skin strained smoothly and exhibited a very low in-plane Poisson's ratio. Actuation frequencies of roughly 1 Hz were achieved.

This work was then extended to a full morphing UAV-scale wing suitable for testing in a wind tunnel. The system was assembled as designed and demonstrated its ability to increase span by 100% while maintaining a constant chord. Wind tunnel tests were conducted at cruise (105 kph) and maximum speed (130 kph) conditions of a candidate UAV test platform, at  $0^\circ$ ,  $2^\circ$ , and  $4^\circ$  angles-of-attack, and at 0%, 50%, and 100% extensions. At each test point, image processing was used to determine the maximum out-of-plane deflection of the skin between ribs. Across all tests, the maximum discernible out-of-plane deflection was little more than 0.5 mm, indicating that a viable aerodynamic surface was maintained throughout the tested conditions.

## 8. Acknowledgement

This work was sponsored by the Air Force Research Laboratory (AFRL) through a Phase I STTR (contract number FA9550-06-C-0132), and also by a Phase I SBIR project from NASA Langley Research Center (contract number NNX09CF06P).

## 9. References

- Agarwal, B. D., Broutman, L. J., and Chandrashekhara, K. (2006). *Analysis and Performance of Fiber Composites*, John Wiley & Sons, Hoboken.
- Bae, J.S., Seigler, T.M. and Inman, D.J. (2005). "Aerodynamic and Static Aeroelastic Characteristics of a Variable-Span Morphing Wing," *Journal of Aircraft*, 42(2): 528-534. doi: 10.2514/1.4397
- Barbarino, S., Bilgen, O., Ajaj, R.M., Friswell, M.I., and Inman, D.J. (2011). "A Review of Morphing Aircraft," *Journal of Intelligent Material Systems and Structures*, 22: 823-877. doi:10.1177/1045389X11414084.
- Bubert, E.A., Woods, B.K.S., Lee, K., Kothera, C.S., and Wereley, N.M. (2010). "Design and Fabrication of a Passive 1D Morphing Aircraft Skin," *Journal of Intelligent Material Systems and Structures*, 21(17):1699-1717 doi: 10.1177/1045389X10378777
- Buseman, A. (1935) "Aerodynamic Lift at Supersonic Speeds," Ae. Techn. 1201, Report No. 2844 (British ARC, February 3, 1937), Bd. 12, Nr. 6: 210-220.
- Bye, D.R. and McClure, P.D. (2007). "Design of a Morphing Vehicle," *48th AIAA Structures, Structural Dynamics, and Materials Conference*, 23-26 April, Honolulu, HI, Paper No. AIAA-2007-1728.
- Chaves, F. D., Avila, J., and Avila, A. F. (2003). "A morphological study on cellular composites with negative Poisson's ratios," *44th AIAA Structures, Structural Dynamics, and Materials Conference*, Norfolk, VA, Paper No. AIAA 2003-1951.
- Evans, K.E., Nkansah, M.A., Hutchinson, I.J., and Rogers, S.C. (1991). "Molecular network design," *Nature*, 353: 124.
- Flanagan, J.S., Strutzenberg, R.C., Myers, R.B., and Rodrian, J.E. (2007). "Development and Flight Testing of a Morphing Aircraft, the NextGen MFX-1," *AIAA Structures, Structural Dynamics and Materials Conference*, Honolulu, HI. Paper No. AIAA-2007-1707.
- Gern, F.H., Inman, D.J., and Kapania, R.K. (2002). "Structural and Aeroelastic Modeling of General Planform Wings with Morphing Airfoils," *AIAA Journal*, 40(4): 628-637. doi: 10.2514/2.1719
- Gevers, D.E. (1997). "Multi-purpose Aircraft," US Patent No. 5,645,250.
- Gibson, L. J. and Ashby, M. F. (1988). *Cellular Solids: Structure and Properties*, Pergamon Press, Oxford.
- Gomez, J. C., and Garcia, E. (2011). Morphing unmanned aerial vehicles. *Smart Materials and Structures*, 20(10):103001. doi:10.1088/0964-1726/20/10/103001
- Hetrick, J. A., Osborn, R. F., Kota, S., Flick, P. M., and Paul, D. B. (2007). "Flight Testing of Mission Adaptive Compliant Wing," *48th AIAA Structures, Structural Dynamics, and Materials Conference*, Honolulu, HI, Paper No. AIAA 2007-1709.
- Joo, J.J. Reich, G.W. and Westfall, J.T. (2009). "Flexible Skin Development for Morphing Aircraft Applications Via Topology Optimization." *Journal of Intelligent Material Systems and Structures*, 20(16):1969-1985.
- Kothera, C.S., Woods, B.K.S., Bubert, E.A., Wereley, N.M., and Chen, P.C. (2011). "Cellular Support Structures for Controlled Actuation of Fluid Contact Surfaces." U.S. Patent 7,931,240. Filed: 16 Feb 2007. Issued: 26 Apr 2011.
- McKnight, G. Doty, R. Keefe, Herrera, A.G. and Henry, C. (2010). "Segmented Reinforcement Variable Stiffness Materials for Reconfigurable Surfaces." *Journal of*

- Intelligent Material Systems and Structures*, 21:1783-1793, doi:10.1177/1045389X10386399
- Munk, M. M. (1924). "Note on the relative Effect of the Dihedral and the Sweep Back of Airplane Wings," NACA Technical Note 177.
- Olympio, K.R., and Gandhi, F. (2010). "Flexible Skins for Morphing Aircraft Using Cellular Honeycomb Cores," *Journal of Intelligent Material Systems and Structures*, 21:1719-1735, doi:10.1177/1045389X09350331
- Parker, H.J. (1920). "The Parker Variable Camber Wing," Report #77 Fifth Annual Report, *National Advisory Committee for Aeronautics*, Washington, D.C.
- Perkins, D. A., Reed, J. L., and Havens, E. (2004). "Morphing Wing Structures for Loitering Air Vehicles," 45<sup>th</sup> AIAA Structures, Structural Dynamics & Materials Conference, Palm Springs, CA, Paper No. AIAA 2004-1888.
- Sarh, B., (1991). "Convertible Fixed Wing Aircraft," US Patent No. 4,986,493.
- Samuel, J.B. and Pines, D.J. (2007). "Design and Testing of a Pneumatic Telescopic Wing for Unmanned Aerial Vehicles," *Journal of Aircraft*, 44(4) DOI: 10.2514/1.22205
- Shigley, J., Mishke, C., and Budynas, R. (2004). *Mechanical Engineering Design*, McGraw-Hill, New York.
- Thill, C., Etches, J., Bond, I., Potter, K., and Weaver, P. (2008). "Morphing Skins," *The Aeronautical Journal*, 112(1129):117-139.
- Wereley, N. and Gandhi, F. (2010). "Flexible Skins for Morphing Aircraft." *Journal of Intelligent Material Systems and Structures*, 21: 1697-1698, doi:10.1177/1045389X10393157.
- Wereley, N. M. and Kothera, C. S. (2007). "Morphing Aircraft Using Fluidic Artificial Muscles," *International Conference on Adaptive Structures and Technologies*, Ottawa, ON, Paper ID 171.
- Wright, O. and Wright, W. (1906). "Flying-Machine" U.S. Patent 821,393. Filed: 23 Mar 1903. Issued: 22 May, 1906.

IntechOpen



## **Recent Advances in Aircraft Technology**

Edited by Dr. Ramesh Agarwal

ISBN 978-953-51-0150-5

Hard cover, 544 pages

**Publisher** InTech

**Published online** 24, February, 2012

**Published in print edition** February, 2012

The book describes the state of the art and latest advancements in technologies for various areas of aircraft systems. In particular it covers wide variety of topics in aircraft structures and advanced materials, control systems, electrical systems, inspection and maintenance, avionics and radar and some miscellaneous topics such as green aviation. The authors are leading experts in their fields. Both the researchers and the students should find the material useful in their work.

### **How to reference**

In order to correctly reference this scholarly work, feel free to copy and paste the following:

Robert D. Vocke III, Curt S. Kothera, Benjamin K.S. Woods, Edward A. Bubert and Norman M. Wereley (2012). One Dimensional Morphing Structures for Advanced Aircraft, Recent Advances in Aircraft Technology, Dr. Ramesh Agarwal (Ed.), ISBN: 978-953-51-0150-5, InTech, Available from:  
<http://www.intechopen.com/books/recent-advances-in-aircraft-technology/one-dimensional-morphing-structures-for-advanced-aircraft>

**INTECH**  
open science | open minds

### **InTech Europe**

University Campus STeP Ri  
Slavka Krautzeka 83/A  
51000 Rijeka, Croatia  
Phone: +385 (51) 770 447  
Fax: +385 (51) 686 166  
[www.intechopen.com](http://www.intechopen.com)

### **InTech China**

Unit 405, Office Block, Hotel Equatorial Shanghai  
No.65, Yan An Road (West), Shanghai, 200040, China  
中国上海市延安西路65号上海国际贵都大饭店办公楼405单元  
Phone: +86-21-62489820  
Fax: +86-21-62489821

© 2012 The Author(s). Licensee IntechOpen. This is an open access article distributed under the terms of the [Creative Commons Attribution 3.0 License](#), which permits unrestricted use, distribution, and reproduction in any medium, provided the original work is properly cited.

IntechOpen

IntechOpen